Structure of Fission Potential-Energy Surfaces in Complete, Multi-Million-Grid-Point Five-Dimensional Deformation Spaces

P. Möller

P. Moller Scientific Computing and Graphics, Inc., P. O. Box 1440, Los Alamos, NM 87544, USA

and

Theoretical Division, Los Alamos National Laboratory, Los Alamos, NM 87545, USA

A. Iwamoto

Department of Materials Sciences, Japan Atomic Energy Research Institute, Tokai-mura, Naka-gun, Ibaraki, 319-1195 Japan

D. G. Madland

Theoretical Division, Los Alamos National Laboratory, Los Alamos, NM 87545, USA

ABSTRACT: **We calculate complete fission potential-energy surfaces for five shape coordinates: elongation, neck diameter, light-fragment deformation, heavy-fragment deformation, and mass asymmetry for even nuclei in the range $82 \leq Z \leq 100$. The potential energy is calculated in terms of the macroscopic-microscopic model with a folded-Yukawa single-particle potential and a Yukawa-plus-exponential macroscopic model in the three-quadratic-surface parameterization. The structure of the calculated energy landscapes includes multiple valleys leading to different scission configurations. The properties of these valleys and the saddle-points leading into these valleys can be directly related to bimodal fission properties observed in the radium region, in the light-actinide region, and in the fermium region [1–4]. The light-actinide region has been extensively studied here in Japan [2,3].**

1 Introduction

When a heavy nucleus divides into two fragments in nuclear fission, two key aspects of the process have challenged researchers since the discovery of fission more that 60 years ago. First, what is the threshold energy for the reaction and, second, what are the shapes involved in the transition from a single nuclear system to two separated daughter fragment nuclei? These two questions are intimately connected. The energy of a nucleus as a function of shape defines a landscape in a multi-dimensional deformation space. It is the energy of the the lowest mountain pass, or saddle-point, in this landscape, connecting the nuclear ground state with the region corresponding to separated fragments that represents the threshold energy of the fission process.

After the discovery of fission in 1938 by Hahn and Strassmann [5] the phenomenon was almost immediately explained by Meitner and Frisch [6] and by Bohr and Wheeler [7] in terms of a model involving a charged liquid drop with a surface tension. One can

then show that when the atomic number increases, the drop becomes increasingly unstable with respect to deformation and at proton number $Z \approx 100$ stability is completely lost. For slightly lower-Z actinide nuclei the fission *barrier* between the ground-state shape and the separated-fragment configuration is sufficiently small that spontaneous fission, due to quantum-mechanical penetration of the fission barrier, occurs with measurable probability. Fission may also be induced by exciting the nucleus to energies above the barrier energy. In some cases, such as n+^{235}U, thermal neutron capture yields sufficient energy to excite the nucleus above the barrier.

In a pioneering use of the first electronic digital computer ENIAC, Frankel and Metropolis [8] in 1947 explored some key aspects of the liquid-drop model potential-energy landscape. In particular, they determined the shapes of nuclei at the saddle-point threshold energies in the macroscopic model they investigated. However, no macroscopic model such as the liquid-drop model of nuclear fission is able to explain certain features of fission-fragment mass and kinetic-energy distributions. For example:

1. Nuclei near ^{228}Ra exhibit two fission modes. We show as Figs. 1 and 2 examples of the extensive data obtained in reference [1]. In one mode, with the lower threshold energy, the fragment mass distribution is asymmetric and the fragment total kinetic energy is about 10 MeV higher than in the other, symmetric mode. The kinetic energies indicate that the scission configuration is more compact for the asymmetric mode than for the symmetric mode. From the totality of the data Ref. [1] concludes: "Thus it seems that after the gross determination of the symmetric or asymmetric character of fission made already at the barrier, the two components follow a different path with no or little overlap in the development from the barrier to the scission configuration."

2. Most actinide nuclei near the line of β-stability undergo mass-asymmetric fission. The heavy fragment mass is close to 140 from Th to Fm, with the remainder of the mass in the light fission fragment.

3. Also, near the far end of the actinide region fission properties change suddenly and sometimes exhibit a two-mode character in the same nucleus. For example the fragment mass distribution changes suddenly from mass-asymmetric for ^{256}Fm to symmetric for ^{258}Fm and there is a sudden, correlated increase in the fragment kinetic energies by 35 MeV. Examples of fission-fragment total kinetic-energy distributions and mass distributions are shown in Fig. 3.

In the 1960s an improved model for the nuclear potential energy as a function of shape emerged. In this *macroscopic-microscopic* model, the potential energy is the sum of shape-dependent liquid-drop and microscopic terms. Over the past 30 years this model has provided considerable insight on nuclear structure. For example nuclear masses are calculated for nuclei throughout the periodic system to an average accuracy of about 0.7 MeV. Improved descriptions of the fission barrier, for example fission-isomeric states and mass-asymmetric fission saddle points were obtained in this model.

However, since the spurt of insights in the early 1970s no major improvement in the description of the fission potential-energy landscape has been obtained. Many calculations based on 1000 or so grid points have been presented. But, to properly describe the evolution of a single nuclear shape into two fragments[1] of different mass and deformation, for example

---

[1]At the present time we do not treat the approximately one in five hundred fissions that are ternary in the actinide region.
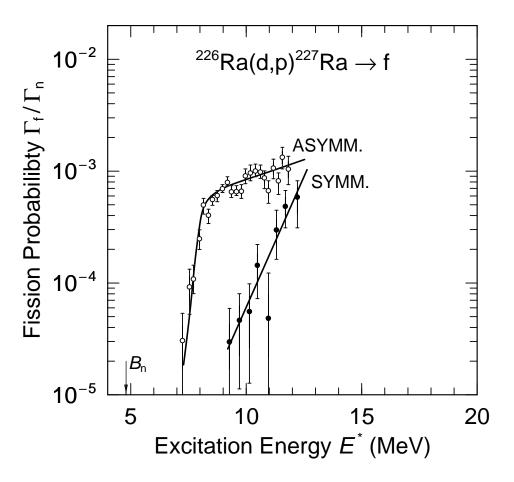
Figure 1: Fission probability data show different thresholds for mass-asymmetric and mass-symmetric fission near ^{227}Ra. The figure is based on a figure in Ref. [1].

one spherical ^{132}Sn-like fragment and one deformed fragment with mass number A near 100, at least five independent shape parameters are required. We have here constructed, calculated, and investigated such a five-dimensional space with $2\,610\,885$ grid-points. Specifically, the five shape coordinates are: (1) charge quadrupole moment, (2) neck diameter, (3) left nascent-fragment deformation, (4) right nascent-fragment deformation, and (5) mass asymmetry. Our potential-energy model is the macroscopic-microscopic finite-range liquid-drop model as defined in Ref. [9] with shape-dependent Wigner and A^0 terms as defined in Ref. [10].

To illustrate the many new features and strengths of our current approach we comment briefly on some aspects of fission potential-energy-surface calculations over the previous 30 years. We then introduce our current model and present some results of our studies of complete five-dimensional potential-energy surfaces.

2   Two-Dimensional Potential-Energy Surfaces

When attending the fission workshop in Kumatori in 1992, I discussed at some length fission in the Fm region. Here, I will briefly recapitulate some of this discussion since it provides a useful background to our new approach. In these previous studies the potential energy was calculated in a two-dimensional deformation space. Some typical shapes in this space are
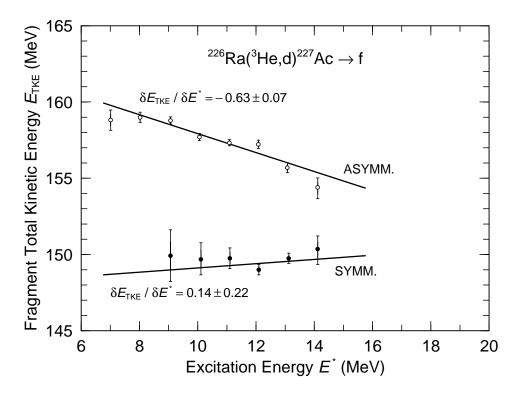
Figure 2: The mass-symmetric and mass-asymmetric fission modes are associated with different average total kinetic energies. The figure is based on a figure in Ref. [1]. The lines are least-squares fits to the data.

shown in Fig. 4. The results obtained for ^{258}Fm are shown in terms of a contour diagram in Fig. 5.

For a long time experimental studies of spontaneous-fission properties in the actinide region showed gradual, predictable changes of such properties as spontaneous-fission half-lives and mass and kinetic-energy distributions as the region of known nuclei above uranium expanded. However, in the 1970s evidence started to accumulate that there were rapid changes in fission properties in the heavy-fermium region. The first observation of the onset of symmetric fission at the end of the periodic system was a study [12] of ^{257}Fm fission. As mentioned earlier, for ^{258}Fm the changes are even more dramatic. Fission becomes symmetric with a very narrow mass distribution, the total kinetic energy of the fragments is about 35 MeV higher than in the asymmetric fission of ^{256}Fm, and the spontaneous-fission half-life is 0.38 ms, compared to 2.86 h for ^{256}Fm. The fission-fragment mass distributions and kinetic-energy distributions of ^{258}Fm and four other heavy nuclei are shown in Fig. 3, taken from Ref. [4]. An important feature of some of the kinetic-energy distributions is that the shape is not Gaussian. Instead, some of the distributions are best described as a sum of two Gaussians. In ^{258}Fm, for example, the kinetic-energy distribution can be represented by two Gaussians centered at about 200 and 235 MeV. This type of fission is referred to as *bimodal* fission.

It has been proposed in Ref. [13] that the rapid change in half-life when going from ^{256}Fm to ^{258}Fm is due to the disappearance of the second saddle in the barrier below the ground-state energy. Fission through only one barrier, the first or inner barrier, gives very good agreement with the observed short half-life of ^{258}Fm [13,14]. However, one may ask if and how the spontaneous-fission half-life is connected to the change in other fission properties at
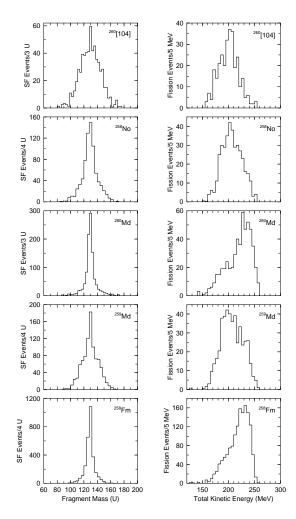
Figure 3: Experimental fission-fragment mass and kinetic-energy distributions for the fission of nuclei close to ²⁶⁴Fm, whose symmetric fragments are doubly magic. The structures of these distributions reflect the valleys, ridges, minima, and saddle points of the underlying nuclear potential-energy surfaces. Taken from Ref. [4].

this transition point, such as the change to symmetric fission and high kinetic energies. We have shown that the old interpretation that the barrier of^{258}Fm has disappeared below the ground state is inconsistent with results from the earlier two-dimensional calculation [10,15] and we have proposed a new mechanism for the short half-life. This previous interpretation is confirmed by our current study.

Although theoretical considerations had far earlier led to suggestions of several fission paths in the potential-energy surface, theoretical spontaneous-fission half-life calculations until rather recently considered only shape parameterizations that allowed for the conventional valley [16–21]. Early calculations that showed, to some extent, the influence of fragment shells at various stages of the fission process, before scission, appeared in the early-to-mid-1970's [22–24].

The first calculation that showed pronounced multi-valley structure *and* predicted the corresponding spontaneous-fission half-lives was performed in Refs. [15,25]. An improved model that also included odd nuclei followed [10]. We show some results from these calculations in Figs. 4 and 5 in units where the radius R_0 of the spherical nucleus is unity.
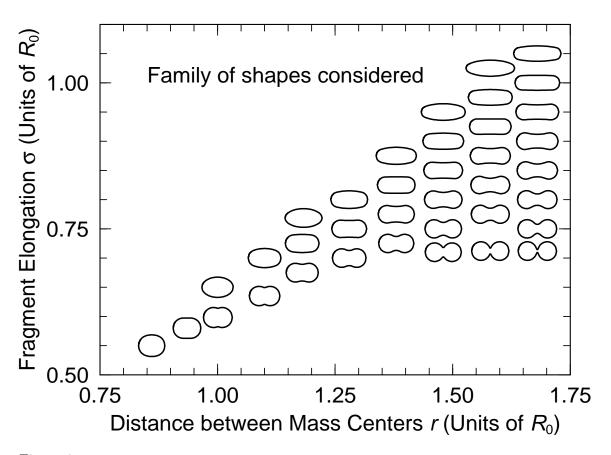
Figure 4: Typical nuclear shapes for which fission potential-energy surfaces are calculated. The selected shapes allow fission into both compact spherical fragments with high kinetic energies and elongated fragments with normal kinetic energies.

These [10,15] showed that some of the good agreement between calculated spontaneous-fission half-lives and measured values obtained in earlier calculations [14,18] for nuclei close to ^{258}Fm was fortuitous.

The high-kinetic-energy fragments in heavy Fm fission were thought to correspond to fission through a scission configuration of two touching spherical fragments, and low-kinetic-energy fission was interpreted as fission through a scission configuration of two elongated fragments. Figure 4 shows a set of shapes that leads from a deformed ground state to both of these scission configurations, and Fig. 5 shows the corresponding calculated potential-energy surface. The three paths are described in the caption to Fig. 5.

3   Common Fallacies in Exploring Multi-Dimensional Fission Potential-Energy Surfaces

Although the results displayed in Figs. 4 and 5 of the previous Section show two fission valleys as was inferred from the experimental data, a severe limitation of the calculation is that only two deformation parameters were included in the study. Only the elongation and neck parameters were varied while the mass asymmetry was kept fixed and the nascent fragment shapes were kept spherical. One asks if the valleys would still appear if these constraints were relaxed. So called "multi-dimensional" calculations have tried to address
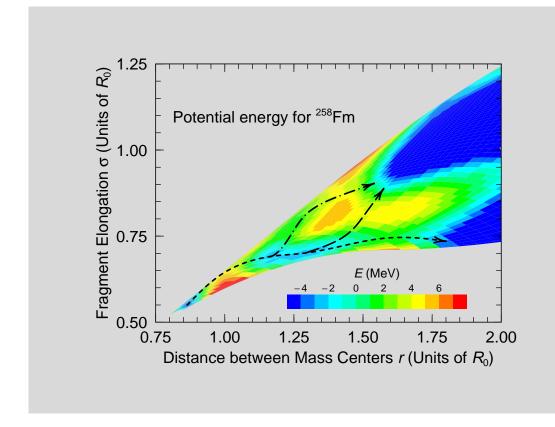
Figure 5: Calculated potential-energy surface for ²⁵⁸Fm, showing three paths to fission. Initially, only one path starting at the ground state exists. Later this path divides into two paths, one leading to compact scission shapes in the lower part of the figure and the other leading to elongated shapes in the upper part of the figure. At a late stage in the barrier-penetration process, a third "switchback path" branches off from the path leading to compact shapes and leads back into the valley of elongated scission shapes. Because this takes place late in the barrier-penetration process, the fission probabilities for fission into compact and elongated shapes are expected to be roughly comparable. Experimentally the probabilities differ by only one order of magnitude. The inertia associated with fission into the lower valley is considerably smaller than the inertia for fission into the upper valley. This calculation is from Ref. [11].

this issue, but most such calculations have been severely flawed.

It is a common misconception that the structure of a multi-dimensional potential-energy function can be determined by calculating and displaying the potential-energy function versus two shape variables, for example, β_2 and β_4 [26] or β_2 and β_3 [27,28], where the potential-energy function has been "minimized" with respect to additional multipoles such as β_4, β_5, β_6 and β_7, or even more multipoles in, for example, Ref. [29]. In fact, such a procedure will yield fictitious saddle points that are either higher or lower than the correct saddle points and with corresponding shapes that are different from the shapes obtained in a correct treatment of the multi-dimensional problem. In Ref. [30] it is shown that a "minimization" procedure does not even work in the simple case of obtaining a one-dimensional fission barrier from a two-dimensional *macroscopic* potential-energy surface. We show in Fig. 6 the surface used as an example in Ref. [30].

The structure of a two-dimensional *macroscopic* potential-energy function is very much simpler than a higher-dimensional *macroscopic-microscopic* potential-energy function. There-
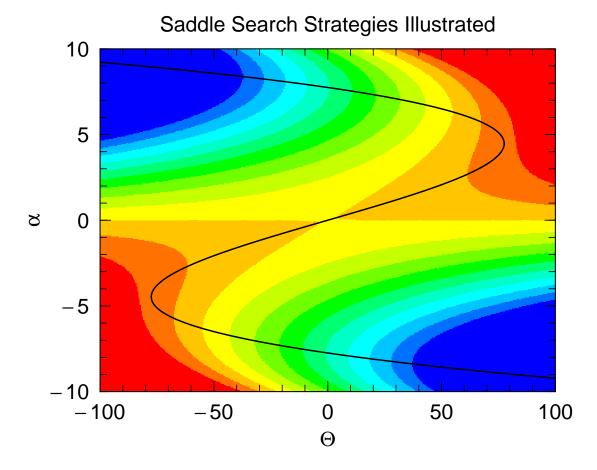
Figure 6: Two-dimensional schematic but realistic surface for which "minimizations" or constrained calculations fail. Blue and cyan colors in the figure represent the lowest energies. The parameter Θ could represent an elongation coordinate in the fission direction and α could represent all other coordinates. The solid line represents valleys and ridges in the surface. If the energy is minimized with respect to α for various fixed elongations, starting on the left side of the plot then initially the upper valley will be followed if, for each successive Θ, the previous value of α is used as a starting coordinate in the minimizations. Towards the right of the figure the upper valley disappears and a discontinuous jump in energy would be obtained when the lower valley floor is obtained as a minimum. This is a typical situation in constrained Hartree-Fock fission calculations. The true saddle point is located in the center of the figure. Similar difficulties occur when a potential-energy function is minimized with respect to higher multipoles and displayed as a function of β_2 and β_3. The structure of the two-dimensional contour plot would have little connection to the full multi-dimensional function. The mathematical representation of this surface was given in Ref. [30].

fore a reduction to a two-dimensional potential-energy surface through a minimization procedure is not a proper method for obtaining the true saddle points of the original multidimensional potential-energy surface. Furthermore, the calculations [26–29] do not account for the shape dependence of the Wigner term as we do here. It is crucial to include such a shape dependence in studies that consider the shape evolution from a single shape to two emerging fragments [10,11,31]. In addition, Refs. [27,28] have without any stated motivation used an inappropriate value $a = 0.56$ fm for the range of the Yukawa-plus-exponential function instead of the standard value $a = 0.68$ fm [32]. The value $a = 0.68$ fm has been determined from adjustments to fusion barrier heights and cannot be arbitrarily changed, because then the agreement between calculated and experimental fusion-barrier heights is

lost. Since saddle-point and scission configurations are close to the shape configuration corresponding to the fusion-barrier peak it is crucial not to lose this agreement.

It is *also* a common misconception that *constrained* self-consistent calculations, for example HF or HFB calculations with Skyrme or Gogny forces [33–35] automatically take into account all non-constrained variables. For the application of saddle-point determination this is incorrect, as we discuss below, and as is very pedagogically explained in Ref. [30]. For one constraint, typically the mass quadrupole moment Q_2, such calculations result in several curves [34], depending on the initial shape at which the calculation is started. These curves may intersect at a cusp. One curve may correspond to a single shape (the fission valley) and another to separated fragments (the fusion valley). The cusp at which these curves intersect is normally *considerably lower* than the true saddle point [30]. The true saddle point is somewhere in the multi-dimensional space between the fusion and fission valley. Also, when two constraints are used in self-consistent calculations, such as quadrupole and octupole constraints in Ref. [35], two or more solutions, or sheets, are obtained. Again, the true saddle point lies somewhere in the multi-dimensional space between these sheets. Therefore, several more carefully selected constraints need to be introduced to accurately locate the saddle points.

It is also of interest to note that in calculations where the potential energy is displayed as contour diagrams versus two shape variables and in which the energy is minimized with respect to additional multipoles, only relatively few points are required to perform a minimization with respect to, say, 3 additional multipoles, about 30 or so. If the two-dimensional contour diagram is based on 10 by 10 points then only 3 000 points are considered in the calculation. In contrast, we consider here for five simultaneous shape-degrees of freedom almost 3 000 000 grid points, that is 1000 *times* more points than earlier calculations purporting to be multi-dimensional.

4   Five-Dimensional Deformation Space

From the above discussion it is clear that to correctly determine the structure of a multi-dimensional fission potential-energy function it is necessary to calculate *a complete hyper-cube or hypervolume* in the multi-dimensional space. Because nascent-fragment shell effects strongly influence the structure of the fission potential-energy surface long before scission, usually already in the outer saddle region, it is crucial to include in calculations the nascent-fragment deformations as two independent shape degrees of freedom. In addition, elongation, neck diameter, and mass-asymmetry shape-degrees of freedom are a minimum required to adequately describe the complete fission potential-energy surface. For nascent-fragment deformations we choose spheroidal deformations characterized by Nilsson's quadrupole ϵ parameter. This single fragment-deformation parameter is sufficient because higher-multipole shape-degrees of freedom are usually of lesser importance in the fission-fragment mass region below the rare-earths.

The three-quadratic-surface parameterization is ideally suited for the above description. In this parameterization the shape of the nuclear surface is specified in terms of three smoothly joined portions of quadratic surfaces of revolution. They are completely specified

[36] by

$$\rho^2 = \begin{cases} a_1{}^2 - \dfrac{a_1{}^2}{c_1{}^2}(z - l_1)^2 \ , & l_1 - c_1 \le z \le z_1 \\[2ex] a_2{}^2 - \dfrac{a_2{}^2}{c_2{}^2}(z - l_2)^2 \ , & z_2 \le z \le l_2 + c_2 \\[2ex] a_3{}^2 - \dfrac{a_3{}^2}{c_3{}^2}(z - l_3)^2 \ , & z_1 \le z \le z_2 \end{cases} \tag{1}$$

Here the left-hand surface is denoted by the subscript 1, the right-hand one by 2 and the middle one by 3. At the left and right intersections of the middle surface with the end surfaces the value of z is z_1 and z_2, respectively. Surfaces 1 and 2 are also referred to as end bodies and, alternatively, nascent fragments below. They are indicated in red in Fig. 7.

There are nine numbers required to specify the expressions in Eq. (1) but the conditions of constancy of the volume and continuous first derivatives at z_1 and z_2 eliminate three numbers. The introduction of an auxiliary unit of distance u through

$$u = \left[\frac{1}{2}\left(a_1{}^2 + a_2{}^2\right) \right]^{\frac{1}{2}} \tag{2}$$

permits a natural definition of two sets of shape coordinates. We define three symmetric coordinates σ_i and three mass-asymmetric coordinates α_i by

$$\sigma_1 = \frac{(l_2 - l_1)}{u}$$

$$\sigma_2 = \frac{a_3{}^2}{c_3{}^2}$$

$$\sigma_3 = \frac{1}{2}\left(\frac{a_1{}^2}{c_1{}^2} + \frac{a_2{}^2}{c_2{}^2}\right)$$

$$\alpha_1 = \frac{1}{2}\frac{(l_1 + l_2)}{u}$$

$$\alpha_2 = \frac{(a_1{}^2 - a_2{}^2)}{u^2}$$

and

$$\alpha_3 = \frac{a_1{}^2}{c_1{}^2} - \frac{a_2{}^2}{c_2{}^2} \tag{3}$$

The coordinate α_1 is not varied freely but is determined by the requirement that the center of mass be at the origin.

When a grid of deformation points is selected in the three-quadratic-surface parameterization, a substantial practical problem is that not all values of the deformation parameters correspond to a physical shape. Another complication is that some of the shape-parameters above are rather indirectly related to more familiar quantities associated with nuclear shape. To generate a reasonable deformation grid in the three-quadratic-surface parameterization we therefore select the input deformations by starting from more familiar concepts.

Five Essential Fission Shape Coordinates

41	Q_2 ~	Elongation (fission direction)
⊗		
20	α_g ~	(M1-M2)/(M1+M2) Mass asymmetry
⊗		
15	ε_{f1} ~	Left fragment deformation
⊗		
15	ε_{f2} ~	Right fragment deformation
⊗		
15	d ~	Neck

⇒ 2 767 500 grid points – 156 615 unphysical points
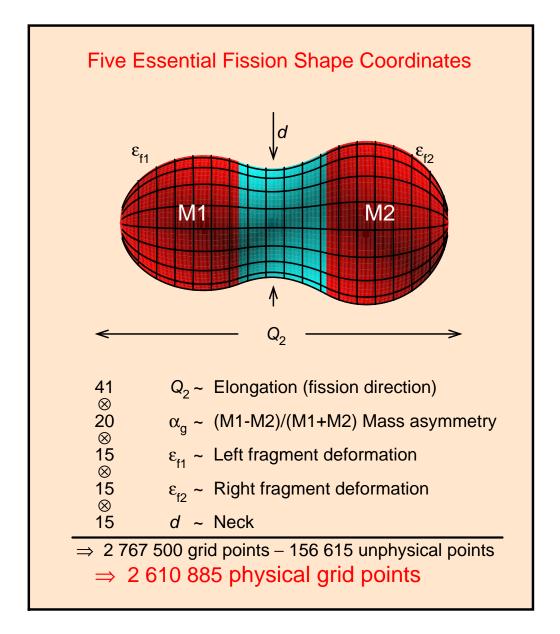
⇒ 2 610 885 physical grid points

Figure 7: Five-dimensional shape parameterization used in the present potential-energy calculation. Different colors indicate the three different quadratic surfaces defined by Eq. (1). The first derivative is continuous where the surfaces meet. Note that we give the charge quadrupole moment Q_2 in terms of ^{240}Pu with the same shape as the nucleus considered, so that the nuclear size effect is eliminated. The end body masses, or equivalently volumes, M_1 and M_2, refer to the left and right nascent fragments were they completed to closed shapes. For the nascent spheroidal fragments we characterize the deformations by Nilsson's quadrupole ϵ parameter.

First, it is reasonable to expect that at some stage of the fission process the shape of the emerging fragments will start to resemble the ground-state shapes of the final fragments. Therefore we want to include in our investigation end-body eccentricities that correspond to known final-fragment shapes in the ϵ parameterization. In terms of the Nilsson perturbed-spheroid ϵ_2 parameter [37–39] we designate the shape of surface 1 by ε_{f1} and the shape of the other end body by ε_{f2}. One can then show that the deformation parameters α_3 and α_3

are connected to ε_{f1} and ε_{f2} by the relations

$$\sigma_3 = \frac{1}{2}\left[\left(\frac{3-2\varepsilon_{f1}}{3+\varepsilon_{f1}}\right)^2 + \left(\frac{3-2\varepsilon_{f2}}{3+\varepsilon_{f2}}\right)^2\right] \tag{4}$$

and

$$\alpha_3 = \left[\left(\frac{3-2\varepsilon_{f1}}{3+\varepsilon_{f1}}\right)^2 - \left(\frac{3-2\varepsilon_{f2}}{3+\varepsilon_{f2}}\right)^2\right] \tag{5}$$

In our present calculation we investigate quadrupole shapes that in terms of ε_{f1} and ε_{f2} correspond to the set

$$\{-0.2, -0.15, -0.1, 0.00, 0.1, 0.15, 0.175, 0.2, 0.225, 0.25, 0.275, 0.3, 0.35, 0.4, 0.5\} \tag{6}$$

This set includes most fission-fragment ground-state shapes. It is not necessary to consider higher multipole components such as ϵ_4 because for ground states below the rare-earths, that is, in the fission-fragment region relevant to this study, higher shape multipoles usually only lower the ground-state by a maximum of 1 MeV, often much less. Thus we have 15 left and right fragment deformations. The set includes the sphere and three oblate shapes.

A common notation used to characterize the fragment mass asymmetry of a fission event is M_H/M_L where M_H and M_L are the masses of the heavy and light fission fragments respectively. For the purpose of grid-point generation for the potential-energy calculation it is convenient to relate a mass-asymmetry shape-degree of freedom for the prescission nucleus to the final fission-fragment mass asymmetry in some fashion, although the final mass division, strictly speaking, cannot be determined from the static shapes occurring before scission. However, the exact nature of our definition of mass asymmetry for a single shape has no effect on the calculated saddle-point energies and shapes because our five-dimensional grid covers all of the physically relevant space available to the 3QS parameterization, regardless of how we choose to define a "mass-asymmetry" coordinate. So that we obtain equations that are reasonably simple to work with for the purpose of grid-point generation, we define an auxiliary grid mass-asymmetry parameter α_g

$$\alpha_g = \frac{M_1 - M_2}{M_1 + M_2} \tag{7}$$

where M_1 and M_2 are the volumes inside the end-body quadratic surfaces, were they completed to form closed-surface spheroids. Thus

$$\alpha_g = \frac{a_1^2 c_1 - a_2^2 c_2}{a_1^2 c_1 + a_2^2 c_2} \tag{8}$$

where a denotes the transverse semi-axis and c the semi-symmetry axis of the left (1) and right (2) quadratic surfaces of revolution. The 3QS parameter α_2 is then completely determined by the relation

$$\alpha_2 = 2\,\frac{\left(\dfrac{(\alpha_g+1)^2\,(\alpha_3+2\,\sigma_3)}{(\alpha_g-1)^2\,(\alpha_3-2\,\sigma_3)}\right)^{1/3}+1}{\left(\dfrac{(\alpha_g+1)^2\,(\alpha_3+2\,\sigma_3)}{(\alpha_g-1)^2\,(\alpha_3-2\,\sigma_3)}\right)^{1/3}-1} \tag{9}$$

for specific values of $\varepsilon_{\mathrm{f1}}$ and $\varepsilon_{\mathrm{f2}}$ of the end bodies, which determine σ_3 and α_3. With this definition we select 20 grid points corresponding to

$$\alpha_{\mathrm{g}} = -0.02 \ldots (0.02) \ldots 0.36 \tag{10}$$

We have closely spaced the asymmetry coordinate so that we will be able to spot favorable saddle-point shapes that may not appear in a more sparsely spaced grid. For ^{240}Pu the values 0.00, 0.02, and 0.36 of the mass-asymmetry coordinate α_{g} correspond to the mass divisions 120/120, 122.4/117.6, and 163.2/76.8, respectively.

Because of the intuitive appeal of the notation $M_{\mathrm{H}}/M_{\mathrm{L}}$ we use it below to characterize the "asymmetry" of a single shape. We then connect M_{H} and M_{L} to α_{g} through

$$M_{\mathrm{H}} = A\frac{1 + \alpha_{\mathrm{g}}}{2} \quad \text{and} \quad M_{\mathrm{L}} = A\frac{1 - \alpha_{\mathrm{g}}}{2} \tag{11}$$

for a nucleus with A nucleons for which the the left fragment is heavier that the right, which is the case for all our examples below. For shapes with a well-developed neck the ratio obtained with this definition can be expected to be close to the final fragment mass-asymmetry ratio. We cannot conveniently use M_1 and M_2 to designate the final fragment mass asymmetries because they do not sum up to the total nuclear volume or mass. Equation (11) simply represents a scaling of M_1 and M_2 so that their sum after scaling adds up to the total mass number A.

We select the deformation parameter σ_1 so that our grid consists of 41 values of the quadrupole moment Q_2. That is, for each combination d, α_{g}, $\varepsilon_{\mathrm{f1}}$, and $\varepsilon_{\mathrm{f2}}$ we determine by a numerical procedure 41 values of σ_1 so that 41 preselected values of Q_2 are obtained.

In the selection of σ_2 values it is useful to observe that for small values of σ_1 there is a minimum neck diameter $d > 0$. At a certain transition point $\sigma_1 = \sigma_{\mathrm{1t}}$ a zero-width neck $d = 0$ can form. This transition configuration, for which the middle body is absent, is the scission configuration of completely formed fragments, or, alternatively the *polar-parallel* [40] touching configuration of colliding heavy ions. For this configuration we find in the completely general case of arbitrary mass asymmetry and end-body eccentricities:

$$\sigma_{\mathrm{1t}} = \frac{\sqrt{\dfrac{\alpha_2\,\alpha_3 - 2\,\alpha_2\,\sigma_3 + 2\,\alpha_3 - 4\,\sigma_3}{\alpha_2\,\alpha_3 + 2\,\alpha_2\,\sigma_3 - 2\,\alpha_3 - 4\,\sigma_3}} + 1}{\sqrt{\dfrac{\alpha_3 - 2\,\sigma_3}{\alpha_2 - 2}}} \tag{12}$$

Because the fission saddle point occurs before scission for heavy systems we do not investigate the separated-fragment configurations that can occur in the region $\sigma_1 > \sigma_{\mathrm{1t}}$. Thus, for $\sigma_1 < \sigma_{\mathrm{1t}}$ the minimum value of σ_2 that we consider is the minimum value allowed by the parameterization, for $\sigma_1 > \sigma_{\mathrm{1t}}$ the minimum value of σ_2 is the value corresponding to the scission configuration. Based on these considerations we select 15 values of σ_2 so that we for each combination of Q_2, $\varepsilon_{\mathrm{f1}}$, $\varepsilon_{\mathrm{f2}}$, and α_g obtain a suitable spacing in the range between the smallest and highest value possible for this highly nonlinear variable.

This choice of deformation coordinates would be expected to yield $2\,767\,500$ grid points in the full 5-dimensional space of the three-quadratic-surface parameterization. In fact, our study completely exhausts the physically relevant space available in this parameterizations. However, shapes corresponding to certain quadrupole moments do not exist for specific combinations of the other shape parameters. For example, zero quadrupole moment cannot

be realized for shapes with very deformed ends. In our grid there exist 156615 such "unphysical" points. Thus we are left with $2\,610\,885$ shapes for which we actually calculate the potential energy.

To summarize, we consider here the physically relevant part of the full 5-dimensional space of the three-quadratic-surface parameterization in terms of 41 values of the charge quadrupole moment Q_2, 15 steps in the neck diameter, 15 values of the fragment deformation ε, where $-0.2 \leq \varepsilon \leq 0.50$ for each of the two nascent fragments, and 20 values of the mass asymmetry $\alpha_{\mathrm{g}} = (M_1 - M_2)/(M_1 + M_2)$, where M_1 and M_2 are the volumes of the left and right nascent fragments were they completed to closed shapes, and where $\alpha_{\mathrm{g}} = -0.02(0.02)0.36$. The various shape coordinates are enumerated in Fig. 7 where also an example of a shape is shown. We have earlier [41] emphasized that it is important to consider a *dense* grid in ε and mass asymmetry because fragment shell corrections vary rapidly in a narrow range of these deformation coordinates. For example, near ^{132}Sn the microscopic corrections vary by 1 MeV for a change of the nucleon number A by 1 unit.

4.1 *Multipole moments*

The electric multipole moment Q_λ for a homogeneously charged, sharp-surface volume is defined by

$$Q_\lambda = 2 \left(\frac{3Z}{4\pi r_0{}^3 A} \right) \int_V r^\lambda P_\lambda(cos\theta) d^3 r \tag{13}$$

In a cylindrical coordinate system, such as the three-quadratic-surface parameterization, this simplifies to

$$Q_\lambda = \left(\frac{3Z}{r_0{}^3 A} \right) \int_V \sqrt{\rho^2 + z^2}\,\lambda\,\rho P_\lambda(\frac{z}{\sqrt{\rho^2 + z^2}})d\rho\,dz \tag{14}$$

In the three-quadratic-surface parameterization the quadrupole moment can be integrated out exactly.

5 Analysis of Calculated Surfaces by Imaginary Waterflow in Five Dimensions

In spaces of high dimensionality there exist different types of equilibrium points where all first derivatives are zero:

1. Minima where all second derivatives or curvatures are positive.

2. Maxima where all second derivatives or curvatures are negative.

3. Other equilibrium points where some second derivatives are positive and some negative. Here we are interested in identifying threshold values for fission which are often referred to as saddle-point energies. At a fission saddle equilibrium point one second derivative is negative and the rest are positive.

Apart from identifying the threshold energy for fission from a calculated multidimensional potential-energy surface, we are also interested in establishing if there are other, higher saddle points that may be related to competing fission modes, such as in the bimodal fission of ^{258}Fm or the different observed fission thresholds in the fission of ^{228}Ra. It is also of interest to establish the shape of the nucleus at the saddle equilibrium points.

The very definition of an equilibrium point suggests that we find them by taking the derivatives of the calculated energy with respect to all deformation variables at each grid-point and identify those points for which the first derivatives are zero. Because the energies are calculated numerically the derivatives would then also have to be determined numerically.

However, this is not an approach that works in practice. Numerical differentiation is a very ill-conditioned problem in the best of times. This normal difficulty is made worse here by the character of the potential-energy function. It is only calculated to finite accuracy, which is considerably lower than the machine accuracy, in fact to about 3 significant digits or 0.1 MeV in the mass units we use. Because the precise choice of which basis functions are used in the diagonalization of the single-particle Hamiltonian depends on deformation there are small discontinuities in the potential energy of the order of 0.05 MeV or so for infinitesimal changes in deformation, at the transition points between different sets of basis functions.

5.1 *Flooding method for saddle-point height determination*

An ingenious method that avoids all the difficulties that would occur in identifying saddle-points in an approach based on numerical differentiation was recently proposed in Ref. [42]. As presented there the method only allows the determination of the fission threshold energy. The method is best explained by use of a two-dimensional picture. We imagine that we have a geographical landscape of minima, maxima and saddle points and that we are looking for the minimum-height pass or saddle-point between two minima of interest, the first being where we are, the second where we want to go. Instead of searching for a saddle point between two minima we may search for a saddle between a minimum, for example the fission isomeric state, and a valley, for example a valley near the scission point. We will sometimes designate the minima or valleys on opposing sides of the searched-for saddle point by "entry point" and "exit point"

We now start to fill the minimum where we are with water up to some level. We define the lowest grid point to be "wet". We then check all immediately surrounding grid points. If they are below the level to which we filled with water the points are marked as "wet". We now repeat the procedure, that is we check the immediate surroundings of all "wet" points and those that are below the filling level are again marked as "wet". The iteration is continued until no more points are found below the filling level. The water level is now raised and the iterations repeated. At some sufficiently high water level the exit point will become wet. This level defines the saddle-point energy.

To obtain an accurate value of the saddle point energy we start by choosing a large spacing between successive filling levels. Once we have reached the level where the exit point becomes wet we start filling from the previous level, but with a decreased spacing. After flowing over to the exit point we can again start from the previous level and fill from there with a spacing that is now further decreased. It is an interesting optimization problem how to chose these successive spacings.

5.2 *Fluctuation method for saddle-point location determination*

The above steps do not provide the saddle-point coordinates, or the indices corresponding to the saddle-point location in the matrix being studied. However, one realizes that once the water has just flowed over the saddle then the distance between the surface of the water and

the saddle point is very small if the spacing between successive levels in the filling process is small. But any matrix grid point along the rim of the water may be equally close or even closer to the surface of the water. Because the energy difference between neighboring grid-points is of the order of 1 MeV and a large number of grid-points lie at the edge of the water, then a point along the edge may accidentally have exactly the same energy as the saddle-point. How often this happens will depend on the details of the calculation. In our case we save the energies at the grid points as formatted files with 3 decimals in units of MeV. One can now argue that if we saved the energies in double precision with more decimals, or saved the energies in double precision in binary format the probability would be very low that this accidental agreement would occur. However, since it can never be excluded we use the following approach to determine with certainty which grid-point is the saddle point:

As mentioned above, we save the energies with three decimals as mass excesses relative to the spherical macroscopic energy. This means that we are normally dealing with a number with five or fewer significant digits. We then use the procedure described in Sect. (5.1) to determine the saddle-point energy and location. In the iterative procedure of several fillings with reduced distances between successive fillings we go down to a distance of 0.001 MeV in the last iteration. When the water level is over the saddle point, that is when the exit point has become wet, then we determine all grid points that lie between the surface of the water and the previous level 0.001 MeV below the surface. Often we find more than one such point. We then save the matrix locations of all such points. The next step is to add a random number to the matrix under study. The magnitude of the number should depend on the number of decimals saved, so for three decimals a suitable random number to add is 0.001*RANF where RANF is a random number $-1 < \text{RANF} < 1$. Then we repeat the saddle point determination, this time increasing the accuracy in the energy determination to a higher accuracy, for example 0.0001 MeV. We then determine the grid points which lie in the last filling interval. The location that is identical to one of the earlier locations is then the saddle-point location. In the extremely unlikely event that two locations are identical to two earlier locations, then one can just repeat the procedure and add a random number with a different seed to the original energy matrix.

5.3 *Dam method for multiple saddle-point identification*

It is also important to determine from the multi-dimensional potential-energy surface if there are multiple saddle-points leading to different fission modes, such as is the case in the bimodal fission of ^{258}Fm and the symmetric-asymmetric fission modes of ^{228}Ra. This can be accomplished by "building a dam" across the succession of saddle regions that are discovered. Specifically after we have determined the first saddle-point energy and location in the matrix under study we proceed in the following way:

The energy at the location corresponding to the saddle point is changed to 10000 MeV, or some other suitably large number, larger than any occurring in the matrix under study. We then determine the saddle-point as above for the new matrix. If the new saddle point is lying next to any point with energy 10000 MeV it is not counted as a distinct saddle point of the original surface and its energy is also raised to 10000 MeV. In the first iteration there is of course only one point with an energy of 10000 MeV, the original, lowest saddle point. Because of a general property of equilibrium points in multi-dimensional spaces two saddle points have to be separated by a maximum. Therefore, once a sufficiently large neighborhood of the original saddle point has been dammed up, the next saddle-point that

is discovered in our iteration process will not lie next to the dam, but will be some distance removed. Thus, a new saddle point will be identified some distance away from the 10000 MeV dam wall after several "saddle points" that were found lying next to the "dam" of 10000 MeV energies during the building of the dam were discarded.

5.4   *Multiple fission-valley structures*

The dam method for identifying additional saddle-points does not show with certainty how they are connected to valleys that may exist further out in the potential-energy landscape. To obtain this information we must perform additional analyses. In particular it is of interest, once the threshold energies for fission have been identified, to establish if structure in the potential-energy surface leads to multi-mode fission, such as that of the well-known three-peaked mass distribution in ^{228}Ra fission [1]. To look for such structure we investigate as a first step if there are valleys of distinctly different character running in the fission direction of increasing Q_2. That is, for 10 or more fixed Q_2 values beyond the outer saddle region, we determine all minima in the remaining 4-dimensional space of the two fragment deformations, neck diameter and mass asymmetry.

We find that there are often two distinct valleys in the region beyond the second saddle region, one corresponding to a mass asymmetry α_g of about $[140 - (A - 140)]/A$ that is preserved along the valley and one corresponding to mass symmetry. To understand the significance of these valleys it is necessary to determine further details about their structure.

A slight modification of the flooding method allows us to determine that separate saddle points provide entries to the two valleys. In the standard flooding strategy an exit point in either of the two valleys gets "wet" as soon as the same specific saddle threshold is exceeded. This is because the water will flow over the lowest saddle point and down the corresponding valley and then, when sufficiently far along in this valley, it will flow backwards up the other valley. Therefore we block the flow at a certain Q_2 value, say 86 b, so that the water does not flow any further. This can be simply accomplished by ignoring points with higher Q_2. In such an approach one valley gets flooded through one saddle point corresponding to a distinct energy and shape and the other valley through another saddle with a distinctly different shape and energy. If the blockage is moved to successively higher Q_2 then the two saddle points remain unchanged until a critical Q_2 is reached, at which the higher of the two saddles disappears and a new saddle appears just at the blocking wall. This happens when we are sufficiently far down the valley that is entered through the lower saddle point so that the ridge separating the two valleys becomes lower than the higher of the two saddle points seen when the valleys were blocked higher up. To determine the height of the ridge between the two valleys along their entire length we study for each fixed Q_2 the remaining 4-dimensional space in which the two valleys correspond to two minima and the ridge to the saddle separating them. We use the flooding algorithm in four dimensions to localize this saddle. These strategies can also be applied to surfaces with more than two valleys.

6   Results

We have calculated five-dimensional potential-energy surface for 138 even-even nuclei from Pb to Fm. We are currently subjecting these surfaces to various types of imaginary water-flow analyses as discussed in the previous section.

As examples of the structures we have found in the calculated 5-dimensional potential-energy surfaces, we show in Figs. 8 and 9 some fission-valley and separating-ridge features
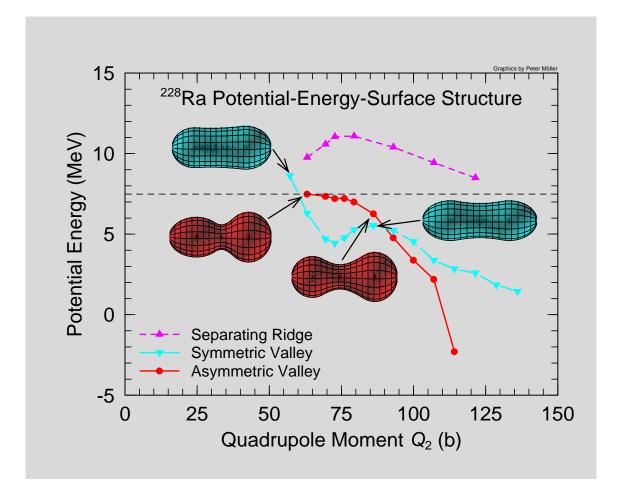
Figure 8: Potential-energy valleys and ridges and corresponding nuclear shapes for ²²⁸Ra. The first point on the two curves with the label "valley" are actually saddle-points at the entrance to the valley that emerges beyond the saddle point. The subsequent points correspond to symmetric or very nearly symmetric shapes. It is of interest to note that the entrance to the symmetric valley is slightly asymmetric. The entry saddle-point to the symmetric valley is 1.13 MeV higher than the entry saddle-point to the asymmetric valley. The highest point on the separating ridge is 2.47 MeV higher than the symmetric saddle. The thin dashed line represents the threshold energy for fission. All energies are given relative to the spherical macroscopic energy.

obtained for ^{228}Ra and ^{232}Th. We also show in Figs. 10 and 11 the mass splits in the mass-asymmetric fission valley. The first point on the fission-valley potential-energy curves in Figs. 8 and 9 is the saddle point for entry into the particular valley. The nuclear shapes corresponding to the saddle points are shown to the left in the figure. Shapes corresponding to the symmetric and mass-asymmetric valleys at $Q_2 = 86$ b are shown to the right. Note that the shape corresponding to the *entry* to the mass-*symmetric* valley is slightly mass-*asymmetric*. The thin dashed line is the calculated threshold potential energy for fission, which to be consistent with the other curves is given relative to the spherical macroscopic energy.

The calculated structure of the potential-energy surface therefore is consistent with the observed bimodal fission features in this region of nuclei [1,2]. The high ridge separating the two valleys for ^{228}Ra is peaked at 2.47 MeV above the entrance saddle to the symmetric
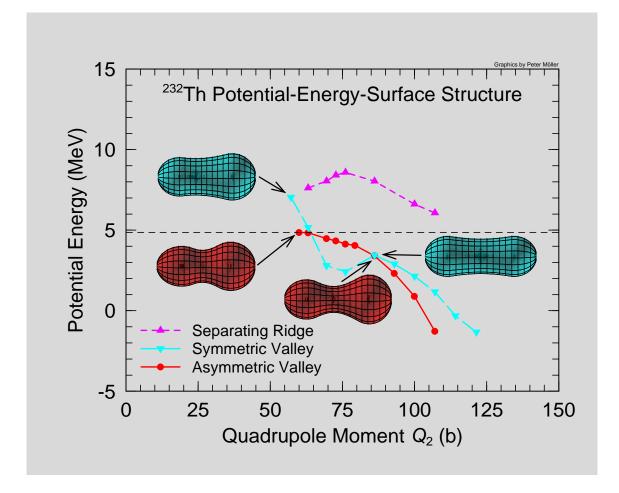
Figure 9: Potential-energy valleys and ridges and corresponding nuclear shapes for ²³²Th. The first point on the two curves with the label "valley" are actually saddle-points at the entrance to the valley that emerges beyond the saddle point. The subsequent points correspond to symmetric or very nearly symmetric shapes. It is of interest to note that the entrance to the symmetric valley is slightly asymmetric. The entry saddle-point to the symmetric valley is 2.17 MeV higher than the entry saddle-point to the asymmetric valley. The highest point on the separating ridge is 1.56 MeV higher than the symmetric saddle. The thin dashed line represents the threshold energy for fission. All energies are given relative to the spherical macroscopic energy.

valley. It therefore keeps the mass-symmetric and mass-asymmetric modes well separated until scission, which is consistent with the experimentally observed data discussed in the introduction. Compare also with Fig. 1. Our results in Fig. 8 are *also* consistent with the observed total fragment kinetic energies which are about 10 MeV higher for asymmetric fission than for symmetric fission for some nuclei in this region, cf. Fig. 2. Because the division into two fragments occurs at higher values of Q_2, corresponding to more elongated scission shape configurations, in the symmetric valley than in the asymmetric valley according to our calculations, the final-fragment kinetic energies can be expected to be higher for the asymmetric fission mode than for the symmetric fission mode, in agreement with Fig. 2.

For ²³²Th the lower separating ridge, peaked at 1.56 MeV above the entrance saddle to the symmetric valley, allows the symmetric component to partially revert back to the asymmetric valley before scission for ²³²Th. Therefore, there is only a very weak symmetric
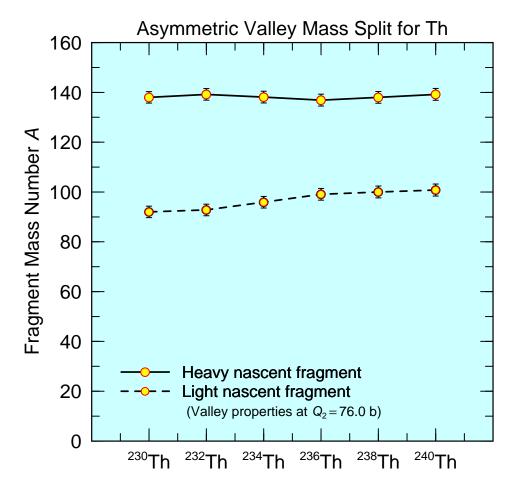
Figure 10: Mass divisions in asymmetric fission for a sequence of Th isotopes from ²³⁰Th to ²⁴⁰Th. The results are in excellent agreement with the experimental observation of a constant-mass heavy fragment at mass number $A \approx 140$ and a light fragment mass corresponding to the remainder of the mass of the original fissioning nucleus.

fission component in low-energy fission of ^{232}Th. We find that the existence of at least two paths in the five-dimensional potential-energy surface is a general result for nuclei in this region and we are now exploring their relative importance over the large range of nuclei for which we have calculated potential-energy surfaces. We note that experimental fission data in the light-actinide region are interpreted in terms of two fission paths, one mass symmetric and one mass asymmetric. The saddle leading to mass-symmetric division is found to be one to two MeV higher than the saddle leading to mass-asymmetric division for nuclei in this region, in excellent agreement with our calculated potential-energy surfaces. Also, the experimental total fragment kinetic energies are higher in asymmetric fission than in symmetric fission. These observations [2,3] are consistent with the compact and elongated shape configurations that we obtain in the corresponding fission valleys.

As we pointed out in the introduction it is a long-standing observation that in binary fission actinide nuclei preferentially divide into one fragment of about mass 140 and a complementary, smaller fragment of mass $A - 140$, where A is the mass number of the original nucleus. We show in Fig. 10 our calculated results for the mass divisions in fission along the thorium isotope chain. For all isotopes we have by the imaginary water-flow technique identified the fission valley corresponding to mass-asymmetric fission at $Q_2 = 76$
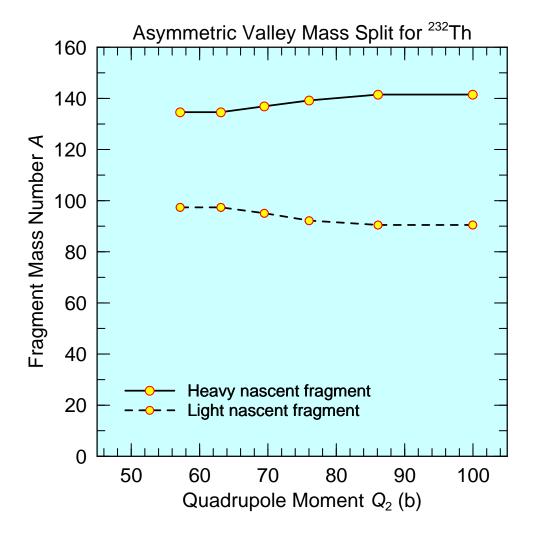
Figure 11: Mass division of the emerging fragments in the asymmetric fission valley for ²³²Th for various quadrupole moments between the saddle and scission points. The values vary only slightly along the valley and converge towards values that are in excellent agreement with the observed peaks of the fragment mass distributions.

b. The value of the mass-asymmetry coordinate α_g at the valley bottom directly yields the mass of the heavy and light fission fragment according to Eq. (11). The "valley floor" corresponds to a local minimum in the four-dimensional space remaining when Q_2 is fixed at a specific value. To show that the results do not depend significantly on the value of Q_2 selected, we show in Fig. 11 the calculated fragment asymmetries that are obtained for a range of Q_2 values for the isotope ^{232}Th. The values remain quite stable, in particular for large values of Q_2.

Nuclei in the region near ^{258}Fm also exhibit bimodal features in fission as discussed in [4]. We have earlier tentatively identified bimodal structures in calculated *two-dimensional* potential-energy surfaces [10,15], but it remained until now to verify that these interpretations are still valid when the calculation is taken from two to five dimensions. In the Fm region we have used one of the imaginary water-flow techniques described previously, namely the dam method, to find alternative saddle points that are higher in energy than the lowest threshold saddle point. For ^{256}Fm and ^{258}Fm we find the two distinct classes of saddle points shown in Fig. 12. For ^{256}Fm the shape of the lowest saddle indicates it
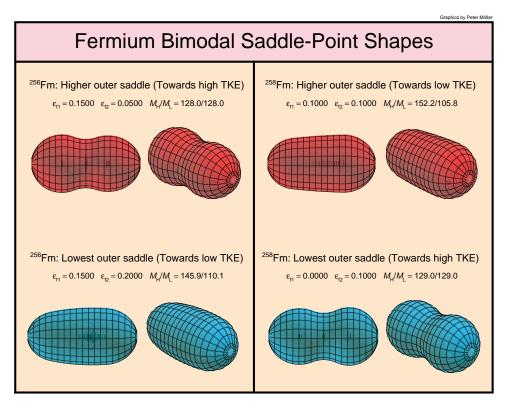
Figure 12: Multiple, bimodal saddle-point shapes for ^{256}Fm and ^{258}Fm based on the grid used in Ref. [41].

corresponds to normal, low-TKE fission similar to what is observed in fission of slightly lighter actinides. However, another saddle point exists, which we calculate to be 0.30 MeV higher than the lower saddle point. This may correspond to fission into compact scission configurations with high kinetic energies. For ^{258}Fm the latter type of saddle-point becomes the lowest saddle point. Thus, we reproduce the experimentally observed transition point between asymmetric low-TKE fission and symmetric high-TKE fission as observed experimentally [4].

7   Summary

The above analysis of our calculated potential energy landscapes in five dimensions allows us to draw the following conclusions:

1. Multiple fission paths are found for most nuclei.

2. For radium and light actinide nuclei two paths are dominating: one mass-asymmetric and one mass-symmetric. These paths correspond to different fission modes, such as those illustrated in Figs. 1 and 2 in the Introduction.

3. The difference in energy between the symmetric and asymmetric saddle-points in our calculated potential-energy surfaces is one to two MeV, which is consistent with the experimentally deduced differences of one to two MeV in threshold energies for these two modes.

4. The shapes we calculate for nuclei evolving in the mass-asymmetric and mass-symmetric valleys are consistent with the total fragment kinetic energies observed for these modes.

5. The long observed mass split in mass-asymmetric fission with a constant heavy fragment mass near $A = 140$ is reproduced convincingly in our calculations.

These results have been obtained in our standard finite-range liquid-drop potential-energy model, which is also applied to the calculation of nuclear masses. No change in the model or its parameters have been made in the current calculation, relative to its 1992 specification in Ref. [9].

The HPC calculations on which the results in this paper are based were carried out on the alpha cluster of 4 CPUs at the TANDEM accelerator in JAERI in the winter of 1998–1999 and subsequently on the 140 AVALON cluster of alpha CPUs at Los Alamos. Results of the investigations at JAERI are discussed in Ref. [41]. This research is supported by the US DOE under contract W-7405-ENG-36.

References

1) E. Konecny, H. J. Specht, and J. Weber, Proc. Third IAEA Symp. on the Physics and Chemistry of Fission, Rochester, 1973, vol. II (IAEA, Vienna, 1974) p. 3.

2) Y. Nagame, I. Nishinaka, K. Tsukada, S. Ichikawa, H. Ikezoe, Y. L. Zhao, Y Oura, K. Sueki, H. Nakahara, M. Tanikawa, T. Ohtsuki, K. Takamiya, K. Nakanishi, H. Kudo, Y. Hamajima, and Y. H. Chung, Radiochimica Acta, **78** (1997) 3.

3) Y. L. Zhao, I. Nishinaka, Y. Nagame, M. Tanikawa, K. Tsukada, S. Ichikawa, K. Sueki, Y. Oura, H. Ikezoe, S. Mitsuoka, H. Kudo, T. Ohtsuki, and H. Nakahara, Phys. Rev. Lett. **82** (1999) 3408.

4) E. K. Hulet, J. F. Wild, R. J. Dougan, R. W. Lougheed, J. H. Landrum, A. D. Dougan, M. Schädel, R. L. Hahn, P. A. Baisden, C. M. Henderson, R. J. Dupzyk, K. Sümmerer, and G. R. Bethune, Phys. Rev. Lett. **56** (1986) 313.

5) O. Hahn and F. Straßmann, Naturwiss. **27** (1939) 11.

6) L. Meitner and O. R. Frisch, Nature **143** (1939) 239.

7) N. Bohr and J. A. Wheeler, Phys. Rev. **56** (1939) 426.

8) S. Frankel and N. Metropolis, Phys. Rev. **72** (1947) 914.

9) P. Möller, J. R. Nix, W. D. Myers, and W. J. Swiatecki, Atomic Data Nucl. Data Tables **59** (1995) 185.

10) P. Möller, J. R. Nix, and W. J. Swiatecki, Nucl. Phys. **A492** (1989) 349.

11) P. Möller and J. R. Nix, J. Phys. G: Nucl. Part. Phys. **20** (1994) 1681.

12) J. P. Balagna, G. P. Ford, D. C. Hoffman, and J. D. Knight, Phys. Rev. Lett. **26** (1971) 145.

13) J. Randrup, C. F. Tsang, P. Möller, S. G. Nilsson, and S. E. Larsson, Nucl. Phys. **A217** (1973) 221.

14) J. Randrup, S. E. Larsson, P. Möller, S. G. Nilsson, K. Pomorski, and A. Sobiczewski, Phys. Rev. **C13** (1976) 229.

15) P. Möller, J. R. Nix, and W. J. Swiatecki, Nucl. Phys. **A469** (1987) 1.

16) P. Möller, Nucl. Phys. **A192** (1972) 529.

17) P. Möller and J. R. Nix, Nucl. Phys. **A229** (1974) 269.

18) A. Baran, K. Pomorski, A. Łukasiak, and A. Sobiczewski, Nucl. Phys. **A361** (1981) 83.

19) G. A. Leander, P. Möller, J. R. Nix, and W. M. Howard, Proc. 7th Int. Conf. on nuclear masses and fundamental constants (AMCO-7), Darmstadt-Seeheim, 1984 (Lehrdruckerei, Darmstadt, 1984) p. 466.

20) K. Böning, Z. Patyk, A. Sobiczewski, and S. Čwiok, Z. Phys. **A325** (1986) 479.

21) A. Staszczak, S. Pilat, and K. Pomorski, Nucl. Phys. **A504** (1989) 589.

22) U. Mosel and H. W. Schmitt, Phys. Rev. **C4** (1971) 2185.

23) A. Săndulescu, R. K. Gupta, W. Scheid, and W. Greiner, Phys. Lett. **60B** (1976) 225.

24) P. Möller and J. R. Nix, Nucl. Phys. **A281** (1977) 354.

25) P. Möller, J. R. Nix, and W. J. Swiatecki, Proc. Int. School-Seminar on heavy ion physics, Dubna, USSR, 1986, JINR Report No. D7-87-68 (1987) p. 167.

26) S. Čwiok, P. Rozmej, A. Sobiczewski, and Z. Patyk, Nucl. Phys. **A491** (1989) 281.

27) S. Čwiok, W Nazarewicz, J. X. Saladin, W. Plociennik, A. Johnson, Phys. Lett. **B322**, 304 (1994).

28) G. M. Terakopian, J. H. Hamilton, Y. T. Oganessian, A. V. Daniel, J. Kormicki, A. V.Ramayya, G. S. Popeko, B. R. S. Babu, Q. H. Lu, K. Butlermoore, W. C. Ma, S. Čwiok, W. Nazarewicz, J. K. Deng, D.. Shi, J. Kliman, M. Morhac, J. D. Cole, R. Aryaeinejad, N. R. Johnson, I. Y. Lee, F. K. McGowan, J. X. Saladin, Phys. Rev. Lett. **77**, 32 (1996).

29) Y. V. Pyatkov, V. V. Pashkevich, Y. E. Penionzhkevich, V. G. Tischenko, A. V. Unzhakova, H. G. Ortlepp, P. Gippner, C. M. Herbach, W. Wagner, Nucl. Phys. **A624**, 140 (1997).

30) W. D. Myers and W. J. Swiatecki, Nucl. Phys. **A601** (1996) 141.

31) W. D. Myers and W. J. Swiatecki, Nucl. Phys. **A612**, 249 (1997).

32) P. Möller and J. R. Nix, Nucl. Phys. **A361** (1981) 117.

33) S. Åberg, H. Flocard, and W. Nazarewicz, Ann. Rev. Nucl. Sci. **40**, 439 (1990).

34) J. L. Egido, L. M. Robledo, and R. R. Chasman, Phys. Lett. **B393**, 13 (1997).

35) J. F. Berger, M. Girod, and D. Gogny, Nucl. Phys. **A502**, c85 (1989).

36) J. R. Nix, Nucl. Phys. **A130** (1969) 241.

37) S. G. Nilsson, Kgl. Danske Videnskab. Selskab. Mat.-Fys. Medd. **29**:No. 16 (1955).

38) S. G. Nilsson, C. F. Tsang, A. Sobiczewski, Z. Szymański, S. Wycech, C. Gustafson, I.-L. Lamm, P. Möller, and B. Nilsson, Nucl. Phys. **A131** (1969) 1.

39) W. M. Howard and P. Möller, Atomic Data Nucl. Data Tables **25** (1980) 219.

40) A. Iwamoto, P. Möller, J. R. Nix, and H. Sagawa, Nucl. Phys. **A596** (1996) 329.

41) P. Möller and A. Iwamoto, Phys. Rev. **C 61** (2000) 47602.

42) A. Mamdouh, J. M. Pearson, M. Rayet, and F. Tondeur, Nucl. Phys. **A644** (1998) 389.